Engineered Science
DOI: https://dx.doi.org/10.30919/es1853

Overtopping-induced Breach Mechanisms of the Asphalt Concrete Core Dam

Meng Yang,[1,5] Qiming Zhong,[1,2,3,*] Liang Hu,[4] Lucheng Zhang,[1] Rafael Morán,[5,*] Ignacio González[5] and Miguel Á. Toledo[5]

Abstract

This study conducts flume model tests on the overtopping failure of asphalt concrete core dams (ACCDs), considering varying asphalt contents of core walls, environmental temperatures, dam heights to explore breach mechanisms for the first time. Test results show that the overtopping-induced breach process is divided into three stages: backward erosion of dam shell materials on the downstream slope until the first fracture of the core wall, multiple fractures of the asphalt concrete core until the occurrence of peak breach flow, and breach stabilization. The decrease of asphalt content or increase of the environmental temperature resulted in higher peak breach flow and earlier time to peak. These test results were employed to develop a predictive formula for the displacement of the core wall before its first fracture. The dam height significantly affects the peak breach flow but has little impact on the time to peak. A simplified numerical model is developed using the Burgers model, the principle of energy conversion, and fracture mechanics. This model accounts for the deformation and displacement of the asphalt concrete core wall after its exposure, the initial crack length, and the crack growth process. The calculated and test results show good agreement with less than ±15% relative error.

Keywords: Asphalt concrete core dam; Overtopping failure; Model experiments; Fracture mechanism; Numerical model.

Received: 29 July 2025; Revised: 29 September 2025; Accepted: 29 October 2025.
Article type: Research article.

1. Introduction

Embankment dams are widely constructed globally for flood control, power generation, irrigation, and water supply.[1] Based on material and structural characteristics, embankment dams are generally classified as earthen dams, core wall rockfill dams, and concrete face rockfill dams.[2,3] Core wall dams have become an increasingly popular type of embankment dam consisting of an anti-seepage body and rockfill materials.[4,5] Traditionally, the sealing elements of rockfill dams have been cores made of clay material.[6] However, in locations where clay soil is scarce, asphalt concrete is used as a substitute material for constructing core wall dams.[7]

The earliest recorded use of asphalt concrete as an impermeable material dates back to 1893, during the construction of the Diga di Codelago Dam in Italy[8]. The dam, with a height of 18 m, featured a layer of asphalt concrete applied to its upstream slope as a protective face. Since then, due to the plasticity, self-healing capability, impermeability, anti-deformation, and anti-seismic performance of asphalt concrete cores, Asphalt concrete core dams (ACCDs) have gained increasing popularity in engineering applications.[9,10] Over the past 60 years, there has been a global surge in the construction of ACCDs. Examples include the Finstertal Dam in Austria,[11] the Storlomvatn Dam in Norway, the Quxue Dam,[12] and Yele Dam in China (as shown in Fig. S1).[13] Among these, the Quxue Dam, with a maximum height of 174 m, is the highest ACCD in the world.

The properties of asphalt concrete are critical to ensuring

[1] *Department of Geotechnical Engineering, Nanjing Hydraulic Research Institute, Nanjing, 210024, China*
[2] *The National Key Laboratory of Water Disaster Prevention, Nanjing, 210098, China*
[3] *Key Laboratory of Reservoir and Dam Safety, Ministry of Water Resources, Nanjing, 210024, China*
[4] *College of Civil and Transportation Engineering, Hohai University, Nanjing, 210098, China*
[5] *ETSI de Caminos, Canales y Puertos, Universidad Politécnica de Madrid, Madrid, 28040, Spain*
**E-mail:* qmzhong@nhri.cn (Q. Zhong); r.moran@upm.es (R. Morán)

the safe operation of ACCDs, as their mechanical properties are influenced by factors such as environmental temperature and asphalt content. Yu *et al*.[14] observed that asphalt content significantly impacts the properties of asphalt concrete. For instance, as the asphalt content increases from 6.3 to 6.9 %, the dynamic elastic modulus of the asphalt concrete also increases by about 6 to 8%. Piuzzi *et al*.[15] reported that the asphalt content is critical in maintaining the mixture's integrity and ensuring proper bonding between its components. In addition, asphalt is a high-molecular and temperature-sensitive material.[16,17] As temperature increases, the molecular activity rises, adhesion energy between asphaltene-phenol and aggregates decreases,[18] as well as the shear strength and modulus.[19] The failure mode of hydraulic asphalt concrete also varies with environmental temperature, the failure progress of the asphalt concrete depends on environment temperature. When temperature ranges from -30 to 0 ℃, the primary failure mode involves aggregate cracking and debonding between the asphalt mastic and aggregate. When the temperature is between 10 and 30 ℃, cracks propagate along the interface between the aggregate and asphalt mastic, with debonding failure being the dominant mode.[20]

In recent years, climate change has led to an increase in extremely heavy rainfall events. If inflow exceeds the flood control design standard, the risk of dam failure rises. On 31 July 2018, the Sheyuegou Reservoir in Hami City, China, experienced dam overtopping and failure due to heavy rainfall. This incident resulted in 20 fatalities, 8 missing people, and significant economic losses.[21] Recently, numerous studies have been conducted on the overtopping-induced breach mechanisms of embankment dams of various types, including earthen dams,[22] clay core dams,[23] and concrete face rockfill dams.[24,25] Despite extensive research on the properties of asphalt concrete, few reports address the overtopping-induced breach mechanisms of ACCDs. Yang *et al*.[7] conducted small-scale model experiments on the breach processes of ACCDs, and observed the phenomenon of continuous erosion of coarse-grained materials and intermittent failures of the asphalt concrete core during the overtopping-induced breach process of ACCDs. However, the factors that influence the breach mechanisms of ACCDs, such as asphalt content in the core wall, environmental temperature, and dam height, remain unexplored.

This study conducts a series of model tests on ACCDs under the influence of the three aforementioned factors to investigate the breach processes. Based on the experimental results, a simplified numerical model is developed using the Burgers model and fracture mechanics to account for fracture and crack propagation in the asphalt concrete core wall.

2. Overtopping-induced breach model tests of the ACCDs

2.1 The large-scale flume model test system

The overtopping-induced breach model tests of ACCDs were conducted using a large-scale flume model test system (as shown in Fig. S2). The system consisted of three parts: water supply equipment, experimental flume, and tailwater pond. (1) Water supply system: The water flow control system consists of a controller, an electric valve, and an electromagnetic flowmeter. The water is supplied by an underground reservoir with a maximum capacity of 800 m³, ensuring adequate water availability for experiments. The inflow rate is set via the controller, which triggers the opening of the electric valve. The electromagnetic flowmeter monitors the supply flow rate and generates a negative feedback signal. A Programmable Logic Controller (PLC) adjusts the opening degree of the electric valve based on this signal, thereby precisely controlling the upstream inflow. This system enables sustainable and stable provision of inflow rates ranging from 0 to 90 m³/h. The pumped water was temporarily stored in an upstream reservoir, measuring 4.0 m in length and 6.5 m in width. (2) Experimental flume: The rectangular flume's dimensions were 40.0 m in length, 1.5 m in width, and 1.5 m in height to minimize the impact of backflow fluctuations on the breach process. (3) Tailwater pond: The tailwater section included two 20-metre-long flumes designed to store and recycle the experimental water flow.

2.2 Experimental setup

2.2.1 Similarity criterion

The Froud similarity criterion, *i.e.*, Froud number, is a dimensionless number based on gravitational similarity, requiring the equality of the Froud number (F_r) between the model and the prototype. This section derives the geometric and kinematic similarity relationships for relevant physical quantities of the model and the prototype. It is assumed that the transverse scale (along the dam axis direction), longitudinal scale (along the flow direction), and vertical scale (along the water depth direction) are distinct, as shown in Eqs. (1)-(3):

$$\lambda_x = L_p / L_m \tag{1}$$

$$\lambda_y = W_p / W_m \tag{2}$$

$$\lambda_z = H_p / H_m \tag{3}$$

where L, W, and H represent the longitudinal length, transverse length, and vertical length, respectively, and the

subscripts p and m denote the prototype and model, respectively. The geometric and kinematic similarities between the prototype and the dam structure are summarized in the Table 1.

2.2.2 Design of the asphalt concrete cores

Asphalt concrete is a visco-plastic solid material formed by binding graded aggregates and fillers with asphalt. This study utilized #70 asphalt to make the asphalt concrete core, and the gradation of asphalt concrete was determined as follows in Eq. (4):[26]

$$p_i = p_{0.074} + (100 - p_{0.074}) \frac{d_i^r - 0.074^r}{D_{\max}^r - 0.074^r} \quad (4)$$

where p_i is the passing rate through sieve opening d_i; $p_{0.075}$ is the filler content; r is the gradation index; d_i is a specific sieve opening size; $D_{\max}$ is the maximum particle size of aggregates. The indices of the asphalt concrete core are listed in Table 2.

The asphalt and aggregates were mixed uniformly at a temperature of 170 °C based on the specified gradation index, asphalt content, and filler content, as detailed in Table 2. The mixed asphalt concrete was then placed into a mold with a width of 1.5 m and a thickness of 0.01 m, compacted until the void ratio was no greater than 3%, and then cooled and formed.

2.2.3 Design of the model dams

The particle gradation of dam materials for the model experiments was selected based on the Sheyuegou ACCD.[21] The equal replacement and similar grading methods were applied to determine the particle size distribution. The grain size distributions of the experimental model and prototype dam materials are shown in Fig. S3.

Based on the geometric parameters of actual ACCDs, the model dam was constructed in a trapezoidal shape in both longitudinal and cross-sections for each model test. The geometry of the model dam referenced the geometric parameters of the actual dam bodies. For all the model dams, both the upstream and downstream slope ratios were set at 1:2 (Vertical/Horizontal), with the asphalt concrete cores positioned at the center of the dam bodies (Fig. S5). The

Table 1: Summary of similarity relationships for physical quantities.

Physical quantity	Prototype	Model	Scaling relationship
Longitudinal length	L_p	L_m	λ_x
Transverse length	W_p	W_m	λ_y
Vertical length	H_p	H_m	λ_z
Cross-sectional area	A_p	A_m	$\lambda_y\lambda_z$
Volume	V_p	V_m	$\lambda_x\lambda_y\lambda_z$
Velocity	v_p	v_m	$\lambda_z^{0.5}$
Time	t_p	t_m	$\lambda_x\lambda_z^{-0.5}$
Discharge	Q_p	Q_m	$\lambda_y\lambda_z^{1.5}$

Table 2: Indices of the asphalt and asphalt concrete core.

Material	Parameter	Unit	Value
Asphalt	Asphalt penetration grade (25 °C, 100 g, 5 s)	0.1 mm	71
	Asphalt softening point	°C	≥ 47
	Ductility (5 cm/min 10 °C)	cm	76
	Wax content	%	≤ 1.9
	Solubility	%	≥ 99.95
	Density (15 °C)	g/cm^3	1.036
	Density (25 °C)	g/cm^3	1.029
Asphalt concrete core	Asphalt content	%	5.2, 6.0, 6.8
	Gradation index	/	0.4
	Filler content	%	13

geotechnical properties of dam materials are shown in Table 3.

In accordance with the Specifications for Construction of Hydraulic Asphalt Concrete, the asphalt was first heated to 160 °C along with the aggregates. After reaching the designated temperatures, the materials were mixed, spread into molds, and compacted to achieve the required void ratio. The prepared asphalt concrete core wall was subsequently hoisted into the flume and secured on both sides to prevent deformation. During the placement of the upstream and downstream soils, the core wall was kept stable within its fixing molds, which were gradually removed as the soil height increased until the wall was completely embedded (as shown in Fig. S4). For the dam construction, a relative density (D_r) of 0.55 was adopted, and the soils were filled layer by layer to ensure uniform compaction. For each model test, the crest width of the dam was set to 0.1 m, and an initial notch with an inverted trapezoidal shape (5 × 5 × 10 cm, height × bottom width × top width) was excavated at the center of the crest to facilitate the monitoring and analysis of the breach process under overtopping flow.

The inflow rate for each model test was set to 5.0 L/s, and two digital cameras recorded the dam breach process. Camera 1 recorded the depth-wise breach process and monitored the asphalt concrete core deformation from the front view, positioned 3.0 m downstream of the model dam. Camera 2 monitored the stream-wise breach process and recorded the asphalt concrete core deformation from the top view, positioned 1.5 m overhead of the model dam. Based on the hydrostatic pressure principle, professional data acquisition equipment was used for real-time data collection at 5 Hz. Pore pressure gauges were strategically positioned to measure the water depth, enabling reservoir capacity and breach flow discharge calculation.

This study considers the factors influencing the ACCD breach processes (Table 4). For instance, the asphalt contents in the core wall are set to 5.2, 6.0, and 6.8%, respectively. The environmental temperatures are set to 0, 15, and 30 °C, respectively; while the heights of the core walls are set to 0.55, 0.825, and 1.10 m, respectively.

3. General observations

3.1 Breach morphology evolution process

Based on the model tests, the processes of the ACCDs due to overtopping failure can be divided into three stages. Stage I: backward erosion of dam shell materials on the downstream slope until the first fracture of the core wall; Stage II: multiple fractures of the asphalt concrete core until peak breach flow; Stage III: breach stabilization.

In this subsection, the model test T1 is taken as an example, and the breach process of the ACCD in each stage is described as follows. Herein, the moment when the water flow overtops the dam crest is defined as $t = 0$ s.

Stage I ($t = 0$–283 s): the water flow overtops the dam crest and forms a breach channel on the downstream slope of the

Table 3: Geotechnical properties of dam materials.

Dam materials	d_{50} (mm)	ρ_d (g/cm^3)	φ (°)	C_c	C_u
Experiment	4.4	2.05	35.4	0.43	21.17
Prototype	8.8	2.19	38.8	0.65	38.33

Note: d_{50} is the median grain size; ρ_d is the dry density of dam materials; φ is the internal friction angle; C_u and C_c are the uniformity coefficient and curvature coefficient, respectively.

Table 4: Conditions of each model test.

No.	Height of dam (m)	Height of core wall (m)	Thickness of core wall (m)	Environmental temperature (°C)	Asphalt content (%)	Inflow (m^3/h)
S1	0.6	0.55	0.01	15	6.8	18
T1	0.6	0.55	0.01	0	6.8	18
T2	0.6	0.55	0.01	30	6.8	18
A1	0.6	0.55	0.01	15	5.2	18
A2	0.6	0.55	0.01	15	6.0	18
H1	0.9	0.825	0.01	15	6.8	18
H2	1.2	1.10	0.01	15	6.8	18

Note: S1 is the standard control group; T1 and T2 are the experimental groups controlling the variable of environmental temperature; A1 and A2 are the experimental groups controlling the variable of asphalt content; H1 and H2 are the experimental groups controlling the variable of dam height.

dam, causing backward erosion of the dam shell material. Fine particles are washed away by the overtopping flow, roughening the surface of the downstream slope (Fig. S6(a)). Due to the heterogeneous characteristics of dam shell materials, multiple head-cuts form due to the erosion of fine particles and then merge into a single head-cut (Fig. S6(b)). The eroded sediments deposit at the downstream toe of the dam, forming a depositional fan, and the breach morphology evolves into a trumpet-shape (Fig. S6(c)). Because the water head of the overtopping flow is relatively low, accompanied by backward erosion in the longitudinal direction, the downcutting erosion of the breach channel occurs in the cross-section, resulting in the toppling failure at the side slopes of the breach channel. The asphalt concrete core becomes exposed as the backward erosion continues to migrate upstream. With the increase in the exposure area of the core wall, the external loads on the suspended core wall grow, leading to an increase in its curvature (Fig. S6(d)).

Stage II (t = 283–345 s): The transition from Stage I to Stage II is identified when the breach discharge exhibits a sudden acceleration, *i.e.*, when the first derivative of discharge dQ/dt shows a marked increase, indicating the onset of rapid breach development. At t = 283 s, under the combined effect of water and soil pressures, the asphalt concrete core fractures for the first time and is swiftly washed away by the breach flow (Fig. S6(e)). The water head of the overtopping flow increases abruptly due to the failure of the core wall, and the downstream slope undergoes intense erosion from the outburst flow, accompanied by intermittent fractures of the core wall and toppling failures of breach side slopes. This process leads to a rapid development of breach morphology and an increase in breach flow, reaching its peak at t = 345 s (Fig. S6(f)). With the increase in hydraulic force during this stage, the depositional fan is gradually washed away.

Stage III (t = 345–645 s): The transition from Stage II to Stage III is quantitatively determined by the condition that the breach discharge reaches its maximum, namely dQ/dt =0 with a sign change from positive to negative, and d^2Q/dt^2 <0, confirming a local maximum. After multiple fractures of the core wall, the breach depth reaches its peak value. Under the hydraulic force of the outburst flow, the upstream dam shell materials are rapidly washed away by the breach flow, and the depositional fan is eventually eroded, further expanding the area of influence. As the upstream water level declines, the outburst flow gradually diminishes, and the breach process ends. Finally, the breach side slopes become nearly vertical, with the slope angles close to 90° (Fig. S6(h)).

The breach hydrograph and variation of the reservoir water level of model test T1 are shown in Fig. 1, corresponding to each stage of the dam breach process illustrated in Fig. S6.

3.2 Fractures of the asphalt concrete core

During the ACCD breach process, the exposed asphalt concrete core is subjected to pressures from the upstream water and soil. The deformation and fracture process of the asphalt concrete core wall is depicted in Fig. S7.

In Stage I, as the overtopping flow erodes the dam shell materials, the asphalt concrete core gradually becomes exposed, with the length and depth progressively increasing (Fig. S7(a)). The asphalt concrete core bends under the combined pressures from the upstream water and soil, along with the shear force exerted by the overtopping flow (Figs. S7(b) and 7(c)). At t = 283 s, the core wall reaches its critical curvature and begins to crack (Fig. S7(d)).

In Stage II, the intense impact of the breach flow on the downstream slope and the cracked core wall causes the fractures to propagate rapidly, resulting in a mass fracture (t = 285 s) (Fig. S7(e)).

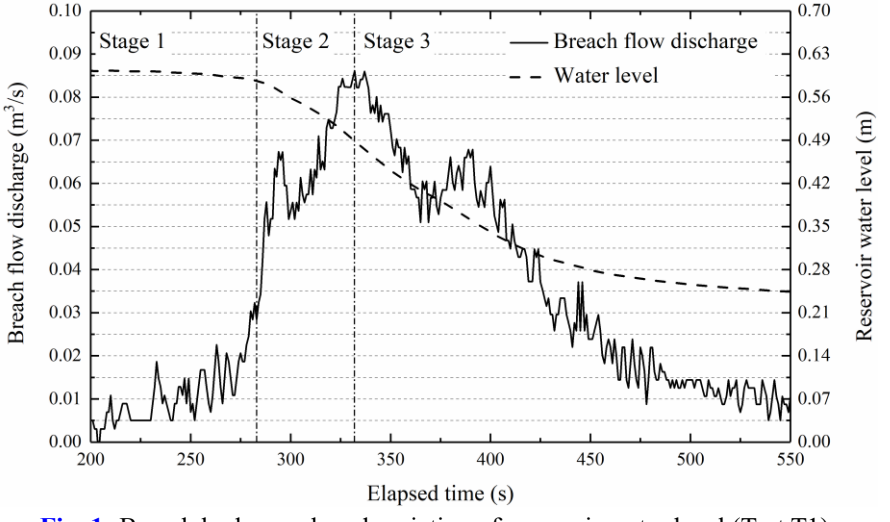

Fig. 1: Breach hydrograph and variation of reservoir water level (Test T1).

In Stage III, the core wall undergoes multiple fractures under the action of the breach flow, continuing until the dam breach process is complete (Fig. S7(f)).

4. Overtopping-induced breach mechanisms of the ACCDs

The ACCDs can exhibit various breach size developments and associated hydrographs under different influencing factors. One of the most relevant factors is the permeability of the downstream shell as it determines the way in which the water flows over the crest under an overtopping event. If the permeability is high, the water goes through the downstream shell.[27-31] The transient seepage network in the shell may lead to local slope instabilities or particle erosion at the toe. The evolution of the downstream shell in this situation has been studied through physics-based numerical modeling or cellular automata.[32,33] When the permeability of the downstream shell is low, most of the water flows over the surface, activating the soil erosion process. This research focuses on a low permeability case as in the physical models most of the water flows over the surface of the downstream shell. The slope is also fixed (2H:1V), to investigate the influence of other factors such as the dam height, asphalt content and environmental temperature in the breaching and failure process (Table 4). Experimental investigations revealed that changing boundary conditions contribute to the overall complexity of the breach process. The evolution of the asphalt core and the downstream shell are fully coupled: the overtopping flow determines the evolution in time of the downstream shell, which determines the breach and the boundary conditions for the core. When the core partially fails, it changes the way in which water flows through the downstream shell. Based on the observations of section 3, this section analyses the influence of various factors on the ACCD breach process by investigating both the breach flow discharges and the breach morphology evolutions, further exploring how these factors affect the failure behavior of the ACCDs.

4.1 Influence of different parameters on breach flow discharge

Before the beginning of the model tests, water flow is pumped into the upstream reservoir. The maximum pumping rate is 90 m³/h, while the experimental period's inflow rate is 18 m³/h (5 L/s). Pore pressure gauges are installed at the upstream dam toe to record the reservoir water level, facilitating the outflow calculation during data analysis. The breach flow discharge is obtained from the following Eq. (5):

$$Q_{\text{out}} = Q_{\text{in}} + \frac{\Delta V}{\Delta t} \tag{5}$$

where Q_{out} is the breach flow discharge; Q_{in} is the inflow rate; ΔV is the variation of water storage in the reservoir; Δt is the time interval.

4.1.1 Asphalt content in the core wall on breach hydrograph

The behavior of the exposed core wall depends on the instantaneous boundary conditions and on the mechanical properties of its material. The latter changes with temperature and asphalt content and the progressive failures of the core play a key role in the whole breach hydrograph. Experiments on the breach processes of ACCDs with different asphalt content ratios were conducted, with values of 5.2, 6.0, and 6.8%, respectively. Fig. 2 indicates a clear decreasing trend in peak breach flow with the increase in asphalt content in the core wall. Higher asphalt content improves the resistance of asphalt concrete against dynamic loads, thereby prolonging its resistance to the erosive impact of upstream overtopping flow, dissipating the upstream hydraulic potential energy, resulting in a lower peak breach flow and a gentler breach hydrograph. The curve slope, which represents the flow increase rate, is influenced by the release of reservoir storage and is further controlled by the damage rate of the asphalt concrete core. Fig. 2 demonstrates that the increase in breach flow discharge begins earliest for the ACCD with an asphalt content of 5.2% at t = 185 s, followed by 6.0% at t = 202 s, and 6.8% at t = 222 s; the corresponding curve slopes are 0.00287, 0.00215, and 0.002, respectively. These results indicate that lower asphalt content reduces the strength of the asphalt concrete core, leading to earlier failure during the experiments.

High asphalt content enhances ductility of the core wall, delaying failure. During breach expansion, the core wall with higher asphalt content exhibits greater displacement, which facilitates the early dissipation of the potential energy in the upstream reservoir. This reduces the peak breach flow and delays its occurrence. The peak flows for ACCDs with asphalt contents of 5.2, 6.0, and 6.8% are 0.1566, 0.1378, and 0.1263 m³/s, occurring at t = 241, 259, and 284 s, respectively. Compared to the core wall with an asphalt content of 5.2%, the peak flows decrease by 12.01 and 19.35% for asphalt contents of 6.0 and 6.8%, respectively, while the corresponding times to peak are delayed by 7.47 and 17.84%.

The results of the Group A experiments show that with increasing asphalt content, the fracture of the core wall was delayed, reduced the upstream water head, and thereby reduced the peak flow. This phenomenon can be accounted for by viscoelastic theory. The asphalt content significantly influences the dynamic modulus (|E*|) of asphalt concrete.[34] When the asphalt content is insufficient, excessive contact

points form between aggregates, resulting in an elevated dynamic modulus and predominantly elastic behavior. This inhibits stress concentration relief at crack tips through viscous dissipation, leading to brittle fracture characteristics. With increasing asphalt content, adequate coating of aggregate surfaces promotes a balanced proportion of viscoelastic components, reducing the dynamic modulus to an optimal range. This enables the material to store energy through elastic deformation and dissipate energy via viscous flow during loading, significantly enhancing ductility and crack resistance.

4.1.2 Environmental temperature on breach hydrograph

For a given asphalt content, the mechanical properties of an exposed core are strongly affected by the environmental temperature. The progressive failure of an exposed core plays a crucial role in the overall breach evolution. Ning *et al.*[16] conducted direct tensile tests on hydraulic asphalt concrete at different temperatures (*i.e.*, 0, 5, 10, 15, and 20 °C). The test results showed that as the temperature decreases from 20 to 0 °C, the tensile strength, tensile modulus, and aggregate cracking ratio increase.

Fig. 3 indicates that three flume model tests are conducted under environmental temperatures of 0, 15, and 30 °C, respectively. The experiment under an environmental temperature of 15 °C has the highest peak breach flow, with a value of 0.1263 m^3/s, while the peak breach flows are 0.0861 and 0.1072 m^3/s for the model tests at environmental temperatures of 0 and 30 °C, with the peak breach flows declining by 31.83 and 15.12%, respectively. On the other hand, for the model test at an environmental temperature of 15 °C, the time to peak is 284 s after the water overtops the dam crest. In comparison, the times to peak for the model tests at environmental temperatures of 0 and 30 °C are 332 and 182 s, delayed by 16.90% and advanced by 35.92%, respectively. The reason is that, under 0 °C conditions, the activity of asphalt molecules declines, and the tensile strength increases.

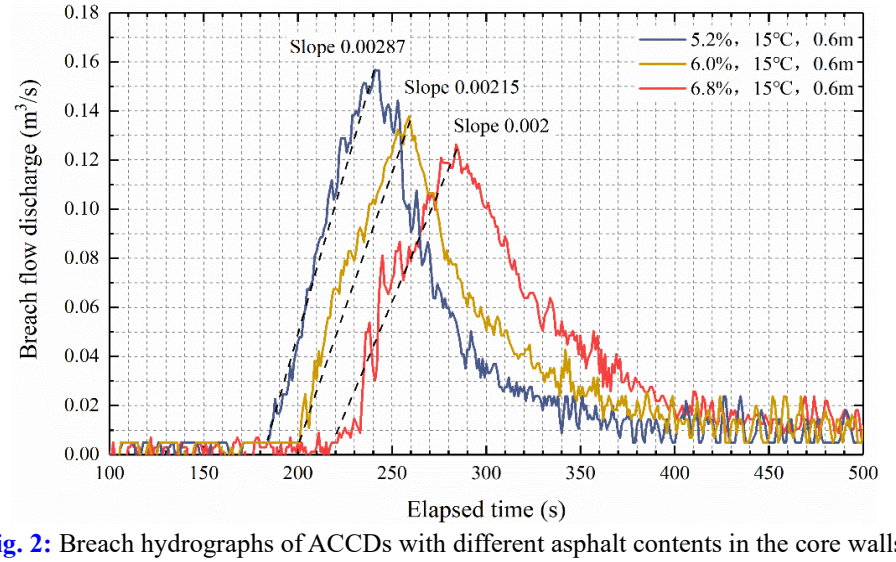

Fig. 2: Breach hydrographs of ACCDs with different asphalt contents in the core walls.

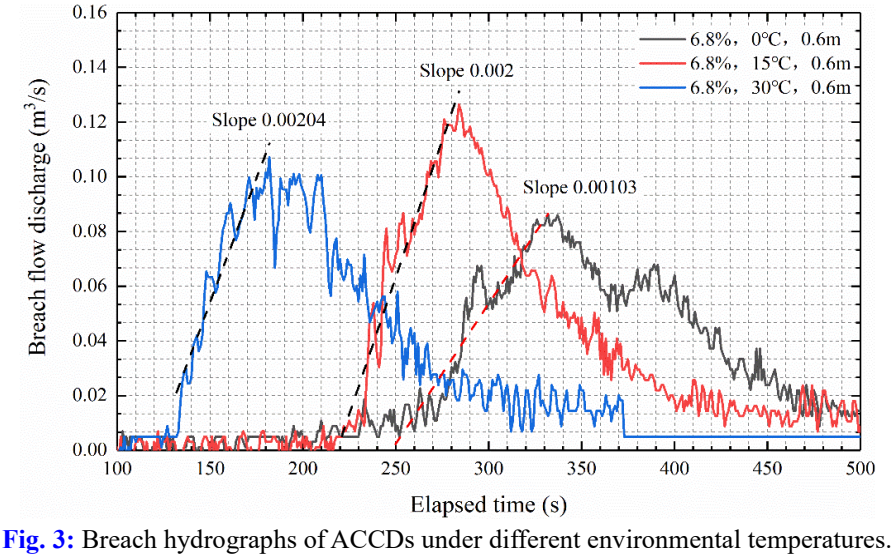

Fig. 3: Breach hydrographs of ACCDs under different environmental temperatures.

The deformation of the asphalt concrete core lasts longer, dissipating more upstream hydraulic potential energy, decreasing the peak breach flow, and delaying the time to peak. Although the model test conducted at an environmental temperature of 15 ℃ exhibits the highest peak breach flow, the time to peak is later compared to the model tests conducted at 30 ℃. Under the condition of 30 ℃, the tensile strength and cohesion of the asphalt concrete decline, causing the failure of the core wall to occur earlier than in the other two model tests. Although the upstream water level at the moment of the initial failure of the core wall is lower compared to the condition at 15 ℃, the reduced strength of the core wall leads to a more rapid failure, resulting in the faster development of breach morphology.

4.1.3 Dam height on breach hydrograph

Experiments were conducted with dam heights of 0.6, 0.9, and 1.2 m, respectively. Fig. 4 indicates that a higher dam increases hydraulic energy. A higher erosion rate of the dam materials enhances the destructive forces acting on the dam body and core wall. Therefore, greater dam heights result in higher peak flow, with values of 0.2534, 0.1722, and 0.1263 m³/s for dams with heights of 1.2, 0.9, and 0.6 m, respectively. The peak breach flow for the dam with a height of 1.2 m is 100.63% larger compared to the 0.6 m dam and 47.15% higher than that of the 0.9 m dam. Fig. 4 shows that the rate of increase in peak breach flow is approximately linearly correlated with dam height.

The differences in breach flow rates induced by varying dam heights can be explained through the erosion processes on the downstream slope. Following overtopping, the downstream slope undergoes surface erosion under the action of overflow, forming multiple-step head-cuts. During retrogressive erosion, the asphalt concrete core becomes exposed, with continuous deepening of the downstream breach depth h_b (Fig. 5(a)).

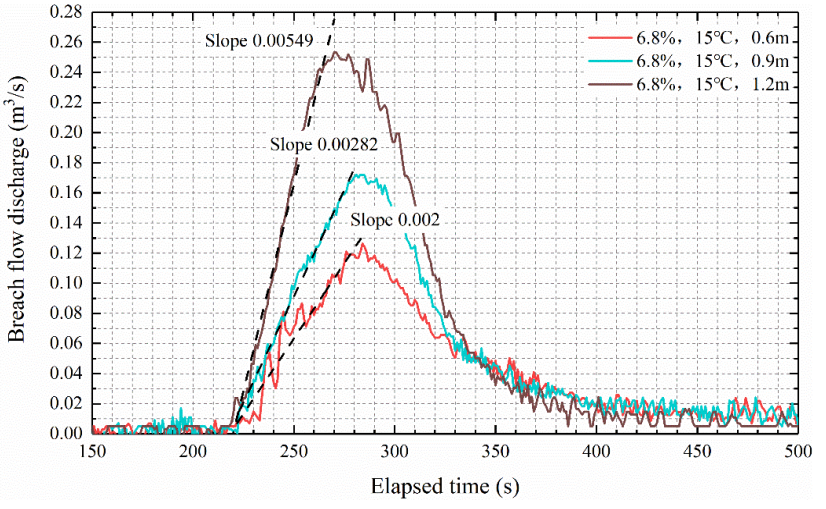

Fig. 4: Breach hydrographs of ACCDs with different dam heights.

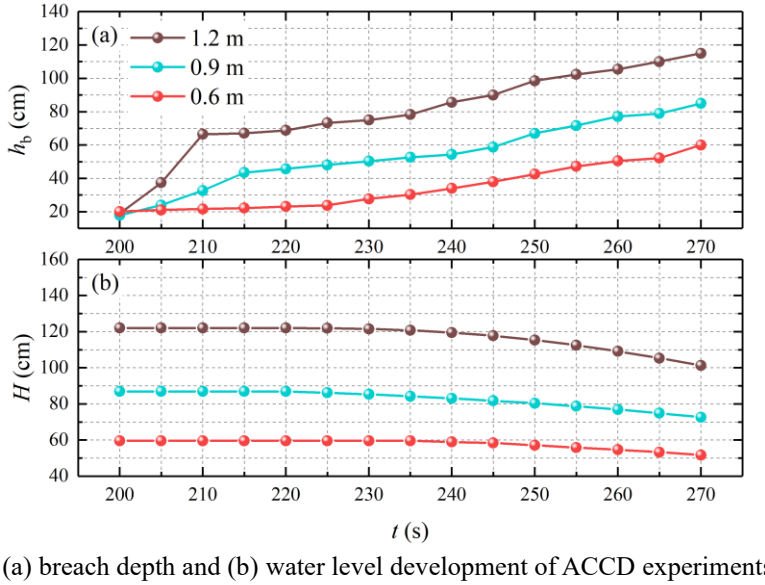

Fig. 5: Temporal evolution of (a) breach depth and (b) water level development of ACCD experiments with different dam heights.

For the 1.2 m-high dam case, its longer slope length allows the overtopping flow to accelerate under gravity during erosion, while the extended erosion duration and flow distance promote the development of multiple head-cuts. The merging of these head-cuts backward erosion to the core, resulting in greater ACC exposure depth compared to the other two test groups. When the asphalt concrete core can no longer resist the combined water and earth pressures, the substantial hydraulic potential energy (H) ruptures the core (Fig. 5(b)), subsequently accelerating slope erosion under breach flow. At this stage, the upstream reservoir capacity becomes the dominant factor controlling the breach discharge hydrograph.

The normalized curves of breach depth-to-water level ratio (as shown in Fig. S8) reveals that before 210 s, the 1.2 m-high dam exhibits rapid increase in downstream breach depth, establishing the prerequisite for subsequent large-scale release of hydraulic potential energy. In contrast, the 0.6 m-high dam group shows an inverse trend in normalized curve compared to the other two cases, primarily because its insufficient hydraulic head prior to ACC failure resulted in limited downstream breach development, while post-ACC failure erosion intensified significantly.

Fig. S8 demonstrates subtle variations in failure processes across different dam heights. The higher dam displays more pronounced slope erosion in early stages, larger ACC failure area, and more violent breach flow due to its fully-developed hydrodynamic conditions.

4.2 Influence of different parameters on breach morphology evolution

The breach processes of ACCDs under an overtopping event differ significantly from those of homogenous or concrete- and asphalt-face embankment dams. It may have similarities with the failure of heterogeneous embankment dams with clay core. However, once the core is exposed the mechanical behavior of an asphalt core can be very different from a clay, and the evolution of ACCD and clay-core embankment dams may differ from each other. The vertical core wall plays a critical structural role during the breach process. As retrogressive erosion of the downstream shell materials exposes the core wall, its structural integrity temporarily halts further upstream erosion, widening the breach. This process continues until external forces compromise the core wall's stability, leading to its failure. Then, the upstream shell materials are eroded by overtopping water flow. This section examines the structural role of the core wall in the breach process under various influencing factors. Key parameters including breach width, depth, and maximum core wall displacement under various influencing factors were analyzed and illustrated in Fig. S9. The downstream slope angle (α) is introduced as a key geometric parameter for trigonometric analysis of breach depth progression during failure processes.

4.2.1 Asphalt content in the core wall on breach morphology evolution

The asphalt content is directly related to the strength of asphalt concrete and significantly affects its strength. After overtopping, the dam shell materials are eroded, and the exposed asphalt concrete core is subjected to upstream water and soil pressures. With increasing asphalt content, the core wall exhibits a stronger ability to resist external loads. Therefore, as asphalt content increases, the curvature of bending increases, and the displacement at the center point of the bent-core wall section also increases. Fig. S10 presents the breach morphologies at the first failure moments of the core walls in the model tests of A1, A2, and S1, illustrating the maximum displacements of the core walls and breach width and depth in the cross-section before the first failure of the core walls.

The detailed measured data of breach sizes before the first failures of the core walls are presented in Table 5, with the relative increments compared to the condition of 6.8% asphalt content. The core wall with an asphalt content of 5.2% exhibits the weakest resistance, with the maximum displacement of the exposed core wall reaching only 1.74 cm before the first failure. In comparison, the maximum displacements of the exposed core wall with asphalt contents of 6.0 and 6.8% are 4.59 and 7.92 cm, respectively. Smaller displacement of the core wall indicates an earlier failure time, resulting in distinct breach morphology at the time of the first failure of the core wall. Due to the weaker resistance of low asphalt content in the core wall, failure occurs earlier, limiting the development of breach width and depth. The breach widths and depths of model tests A1, A2, and S1 are shown in Fig. S10. For the dam with an asphalt content of 6.8% in the core wall, the breach width and depth are 31.3 and 36.4 cm, respectively. In comparison, the breach width and depth of the 6.0% asphalt content core wall are 27.1 and 33.6 cm, decreasing by 13.3 and 7.9%, respectively. The same indices for the 5.2% asphalt concrete core wall are 24.7 and 27.7 cm, decreasing by 21.1 and 24.0%, respectively. These results indicate that the strength of the asphalt concrete core wall follows a nonlinear increasing trend, and asphalt content significantly impacts its structural strength.

To more intuitively illustrate the development of breach width (w) and depth (h_b) under varying influence factors, the variation relationship of the width-to-depth ratio of the breach was investigated. The horizontal axis represents normalized

time, scaled by the duration of Stage 1 to indicate the progression of this stage. The vertical axis displays the breach width-to-depth ratio.

Fig. 6(a) illustrates the width-to-depth ratio of the breach in Group A at the end of the first stage, reflecting the relationship between the rates of breach widening and deepening. T is the total duration of the first stage and t is the real-time of the first stage. Under varying asphalt content, the evolutionary trends during the rapid expansion phase at the end of the first stage are generally consistent. As the breach continues to expand, the core wall undergoes gradual downstream bending deformation under the action of unbalanced earth and water pressures from upstream and downstream sides. Fig. 6(b) illustrates the temporal evolution of the core wall displacement, indicating a significant positive correlation with the progression of the breach enlargement.

4.2.2 Environmental temperature on breach morphology evolution

Asphalt is a temperature-sensitive material. As the temperature increases, asphalt molecules are more easily detached from the aggregate surface under tensile forces.[18] As a result, the environmental temperature plays a role in the progressive failure of the core and the resulting breach

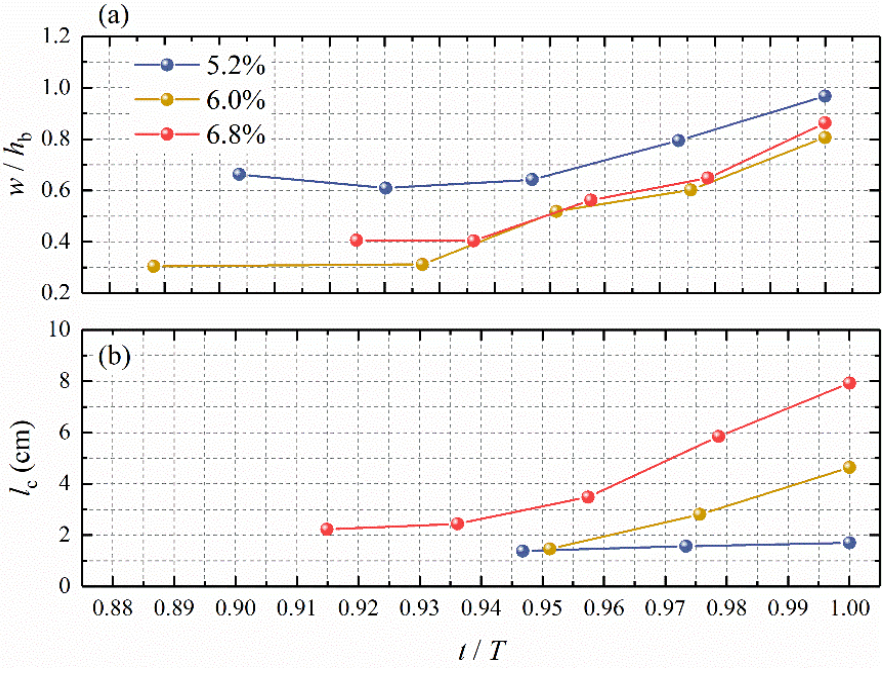

Fig. 6: Temporal evolution of (a) breach expansion and (b) core wall displacement for different asphalt contents.

Table 5: The comparison of breach data of ACCDs with different asphalt contents.

No.	Asphalt content (%)	Failure time (s)	Relative increment	Maximum displacement (cm)	Relative increment	Breach width (cm)	Relative increment	Breach depth (cm)	Relative increment
A1	5.2	188	-20.0%	1.7	-78.5%	24.7	-21.1%	27.7	-24.0%
A2	6.0	205	-12.8%	4.6	-41.8%	27.1	-13.4%	33.6	-7.7%
S1	6.8	235	/	7.9	/	31.3	/	36.4	/

Table 6: The comparison of breach data of ACCDs with different environmental temperatures.

No.	Environmental temperature (°C)	Failure time (s)	Relative increment	Maximum displacement (cm)	Relative increment	Breach width (cm)	Relative increment	Breach depth (cm)	Relative increment
T1	0	283	20.4%	10.2	22.6%	60.0	91.7%	42.3	16.2%
S1	15	235	/	7.9	/	31.3	/	36.4	/
T2	30	130	-44.7%	3.7	-53.2%	12.1	-61.3%	30.0	-17.6%

evolution. The model tests of T1, S1, and T2 involve ACCD breach processes conducted at environmental temperatures of 0, 15, and 30 ℃. Fig. S11 presents the breach morphologies at the first failure moments of the core walls in the three model tests.

The breach data are presented in Table 6, highlighting the significant impact of environmental temperature on the dam breach process. Herein, S1 is also chosen as the representative for comparison to the model tests of T1 and T2. Under the environmental temperature of 0 ℃ in the model test T1, the core wall fractures at $t = 283$ s, representing an increase of 20.4% compared to S1. In contrast, under the environmental temperature of 30 ℃ in the model test T2, the fracture time is significantly advanced to $t = 130$ s, representing an acceleration of approximately 44.7% compared to S1. When the core walls fracture, the central displacement is 10.26 cm at 0 ℃, 7.92 cm at 15 ℃, and 3.72 cm at 30 ℃. The maximum displacement of the core wall before the first failure at 30 ℃ is only nearly one-third of that at 0 ℃.

Regarding breach development, the breach width and depth are 60.0 and 42.3 cm at 0 ℃. In comparison, these values decrease to 31.3 and 36.4 cm at 15 ℃ and further to 12.1 and 30.0 cm at 30 ℃. The breach width shows a significant variation across the three temperatures.

Based on the data in Table 6 and Fig. S11, the maximum displacements of core walls and the breach width and depth in the cross-section before the first failure of the core walls in model tests T1, S1, and T2 indicate that the impact of temperature changes from 0 to 15 ℃ on breach development is less pronounced compared to the impact of changes from 15 to 30 ℃. As shown in Fig. 7, at 0 ℃ and 15 ℃, the breach expansion and core wall displacement exhibit a significant increasing trend. In contrast, under the 30℃ condition, the breach expansion volume and core wall displacement remain relatively small. As can be seen from Table 6, under 30 ℃ conditions, the core wall experiences the earliest failure, occurring at 130s. This behavior can be explained by the temperature-dependent molecular mobility and the resulting evolution of interfacial bond energy.[17] The interfacial interactions between asphalt and silica atoms are predominantly governed by the Lennard-Jones potential and Coulomb potential. An increase in temperature enhances the molecular mobility of asphalt constituents near the silica surface, which reduces the energy barrier associated with the rupture of non-covalent interfacial bonds. Consequently, a degradation in interfacial failure strength is observed.

4.2.3 Dam height on breach morphology evolution

The breach processes under different dam heights varied significantly. Three physical model tests were conducted with dam heights of 0.6, 0.9, and 1.2 m, respectively, while the corresponding maximum displacements of the core wall are 7.9, 5.5, and 5.6 cm. S1 was also chosen as the representative for comparison to the H1 and H2 model tests. Fig. S12 depicts the breach morphologies at the first failure moments of the core walls in the three model tests.

The most significant impact is observed in the breach width and depth. For the dam with a height of 0.6 m, the breach

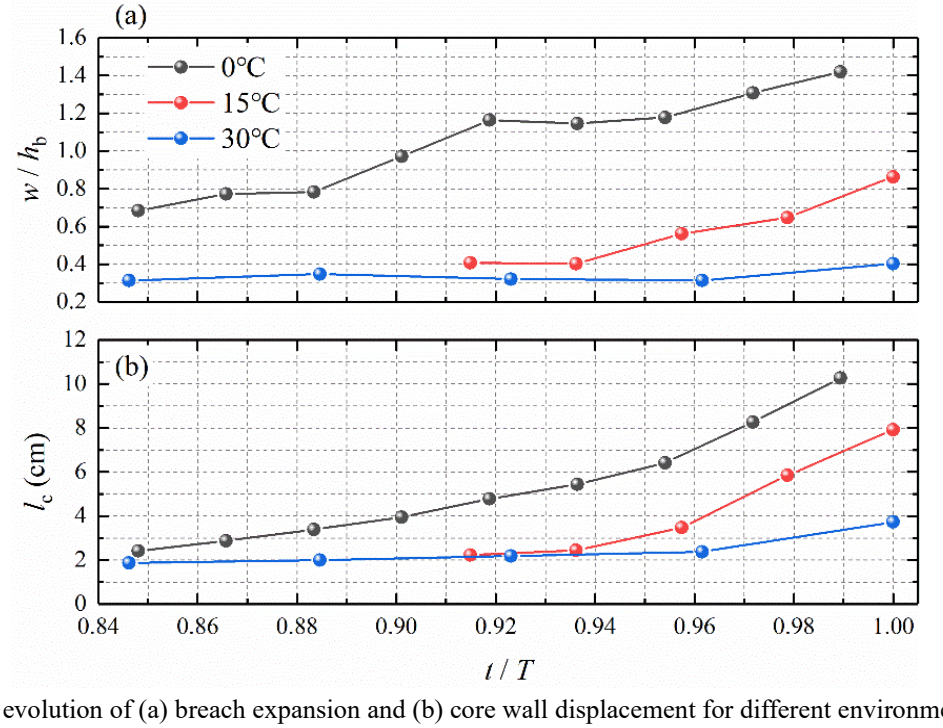

Fig. 7: Temporal evolution of (a) breach expansion and (b) core wall displacement for different environment temperature.

width and depth are 31.3 and 36.4 cm, respectively. In comparison, the corresponding values for the 0.9 m high dam are 14.1 and 40.3 cm, while for the 1.2 m high dam, the values are 13.6 and 56.5 cm, respectively. These results indicate that as the dam height increases, the breach width decreases while the breach depth increases.

Experimental data from varying dam height conditions revealed that different dam heights result in varying erosion depths in the downstream dam shell material, as listed in Table 7. With the increase in dam height, the occurrence of failure time is gradually advanced, and the maximum displacement of the asphalt concrete wall and breach width are decreasing while the breach depth is increasing.

As shown in the Fig. 8, the w/h_b ratio of S1 increases rapidly toward the end of Stage 1, indicating significant breach widening. In contrast, the ratios for H1 and H2 continue to decrease, suggesting that the breach depth increases more substantially compared to the width, accompanied by a concurrent increase in core wall displacement. A detailed depiction of the breach morphology evolution is provided in Fig. 9.

4.3 Elapsed time in each dam breach stage under different conditions

As mentioned in the previous section, the ACCD breach process can be divided into three stages, which depend on the coupling between the evolution of the downstream slope and the resistance of the exposed core. Fig. S13 presents the elapsed time of each stage for each experiment, clearly demonstrating that different factors have varying impacts on each stage.

Stage I is the most sensitive phase affected by different influencing factors. As the water flow overtops, the elapsed time of Stage I is determined by the strength of the core wall, which depends on influencing factors such as environmental temperature, asphalt content in the core wall, and dam height. The environmental temperature (Group T) has the most impact: at 0 ℃, the elapsed time in Stage I is 283 s. At 30 ℃, the

Table 7: The comparison of breach data of ACCDs with different dam heights.

No.	Dam height (m)	Failure time (s)	Relative increment	Maximum displacement (cm)	Relative increment	Breach width (cm)	Relative increment	Breach depth (cm)	Relative increment
S1	0.6	235	/	7.9	/	31.3	/	36.4	/
H1	0.9	227	-3.4%	5.5	-30.4%	14.1	-55.0%	40.3	10.7%
H2	1.2	218	-7.2%	5.6	-29.1%	13.6	-56.6%	56.5	55.2%

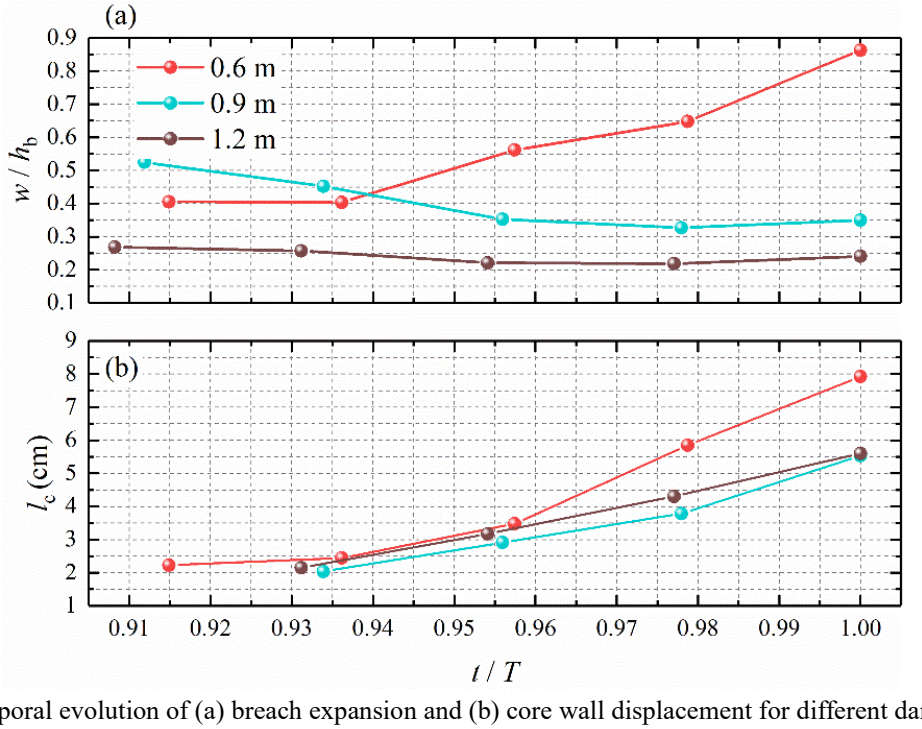

Fig. 8: Temporal evolution of (a) breach expansion and (b) core wall displacement for different dam heights.

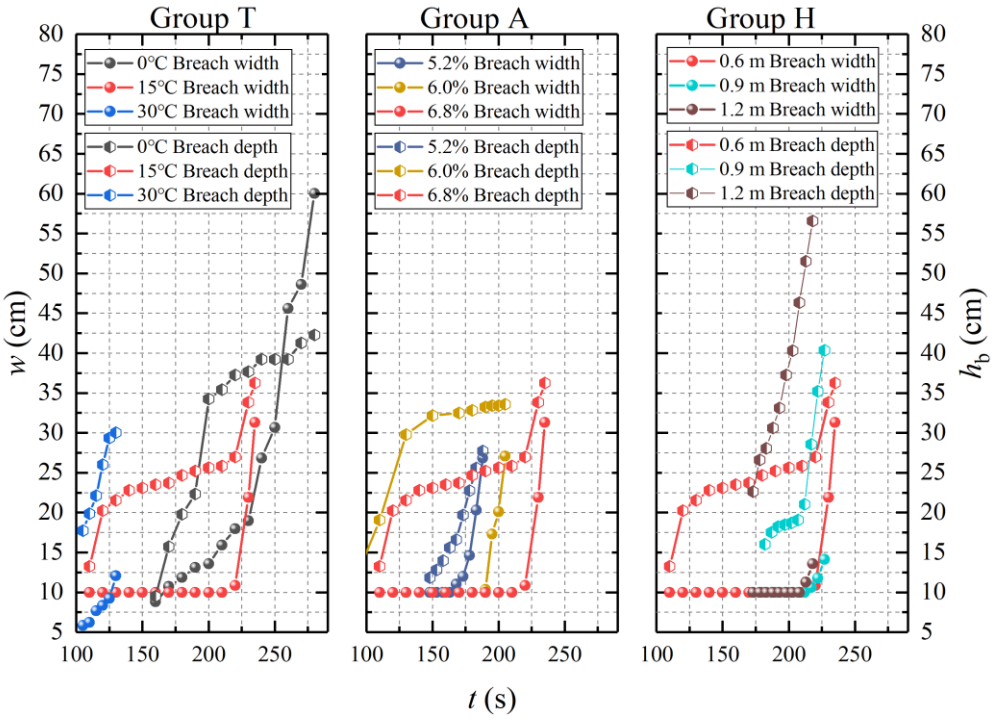

Fig. 9: Development process of breach width and depth on the downstream slope.

corresponding elapsed time is 130 s, representing a 117% reduction. During Stage I, the core wall deforms under external forces, storing energy for its fracture in Stage II.

Stage II begins after the exposed asphalt concrete core's first failure and ends with peak flow. For different influencing factors, the elapsed time of Stage II remains nearly constant. This can be attributed to the adaptability of the core wall's strength to hydrodynamic conditions. In conditions where the core wall has higher strength, the elapsed time of Stage I is longer, with a larger exposed area and higher upstream head potential. In contrast, in conditions with lower core wall strength, the elapsed time of Stage I is shorter, with a smaller exposed area and lower upstream head potential. This results in a similar elapsed time for Stage II.

4.4 Breach development in coarse-grained materials and core wall displacement before its first failure

4.4.1 Breach development process in the coarse-grained materials

For the ACCDs, the development of a breach after overtopping with a low permeability downstream shell represents a complex process that extends beyond mere vertical deepening and lateral widening of the downstream dam shell materials. Data from seven experimental tests were statistically analyzed to investigate breach development in the coarse-grained materials, from the point of core wall exposure to its eventual failure (Fig. 9). Under the erosive effects of the overtopping flow, the downstream slope of the dam forms multiple steep steps that progressively extend upstream until the core wall becomes exposed. The vertical configuration of the core wall transforms the overtopping water, initially in the form of weir flow, into a concentrated jet flow. This jet flow persistently erodes the downstream slope behind the core wall, resulting in undercut scouring of the breach in the coarse-grained materials. During this stage, the breach exhibits minimal lateral expansion. Once a threshold depth within the breach is achieved, further downward erosion ceases, and the jetting flow transitions to scouring the base of the breach, then, the flow washes away the dam shell materials on the downstream slope, leading to the overhang of the upper dam slope due to arching effects, and causing toppling failure and a subsequent lateral expansion of the breach.

Fig. 9 illustrates data from various experimental groups, presented across three separate figures. For Groups T and A, a clear trend is observed where the breach depth develops earlier, and once it reaches the threshold depth, the growth rate slows significantly while the breach width increases sharply. In contrast, the trend exhibited by Group H differs markedly from the other two groups. Specifically, the growth trends of breach depth for experiments with dam heights of 0.9 and 1.2 m do not exhibit the same slowing pattern, as the breach width fails to expand. This difference arises because these dams have relatively greater heights, and the threshold depths in the breaches are not reached by the time the core wall failures occur.

Future studies should focus on deriving a generalized

dimensionless expression for the threshold breach depth based on the balance between hydraulic shear force and sediment incipient motion. Such an expression could integrate key dimensionless parameters such as the Shields number, relative submergence, and dam height-to-particle size ratio, to quantitatively describe the nonlinear relationship observed about the threshold depth. Validating this expression through controlled experiments measuring near-bed velocity and shear stress at the onset of lateral expansion would significantly improve the physical understanding and predictive modeling of breach morphology evolution.

4.4.2 Maximum displacement of the exposed core wall before its first failure

At Stage I, the breach depth increases as the dam materials on the downstream slope were eroded. Upon reaching the threshold depth, the breach in the dam shell materials widens laterally, causing the exposed asphalt concrete core to bend under the unsupported downstream condition, forming an arch-like shape. The evolution processes of the breach width and the displacement of the exposed core wall (l_c) for different model tests during Stage I are presented in Fig. 10. The contour lines of core wall displacement are shown in Fig. S14.

Fig. 10 demonstrates a clear correlation between breach morphology and the displacement of the core wall. Regarding the influencing factor of environmental temperature (Fig. 10(a)), as the environmental temperature increases, the breach width in the dam shell materials decreases, as does the displacement of the core wall before failure due to the reduction in core wall strength.

Fig. 10(b) illustrates the influencing factor of dam height, showing that the most significant impact of varying dam heights is observed in the evolution of breach width, which affects the displacements of the core walls. In this series of experiments, for the dam with a height of 0.6 m, once the breach reaches the threshold depth, it begins to widen laterally. This process allows more time for core wall displacement, resulting in the largest value. For a dam of greater height, the dam shell materials are predominantly eroded by overtopping flow through an undercutting process. Before reaching the threshold depth, the breach size has no significant lateral widening. However, the asphalt concrete core is subjected to increasing upstream water and soil pressures due to the continuously expanding exposed area until Stage I concludes. Therefore, the experimental results for breach width and core wall displacement are comparable.

Fig. 10(c) illustrates the influence of asphalt content in the core wall, showing that varying asphalt contents result in differing strengths of the asphalt concrete core. A core wall with lower asphalt concrete content exhibits reduced strength and is more prone to failure, resulting in smaller displacement and breach width before the initial failure of the core wall.

To facilitate a more intuitive comparison of the development patterns of core wall displacement and breach expansion under varying external influences (Fig. S15), the data from the S1 group experiment were selected as the baseline. The experimental results from other groups were normalized by dividing them by the corresponding S1 data,

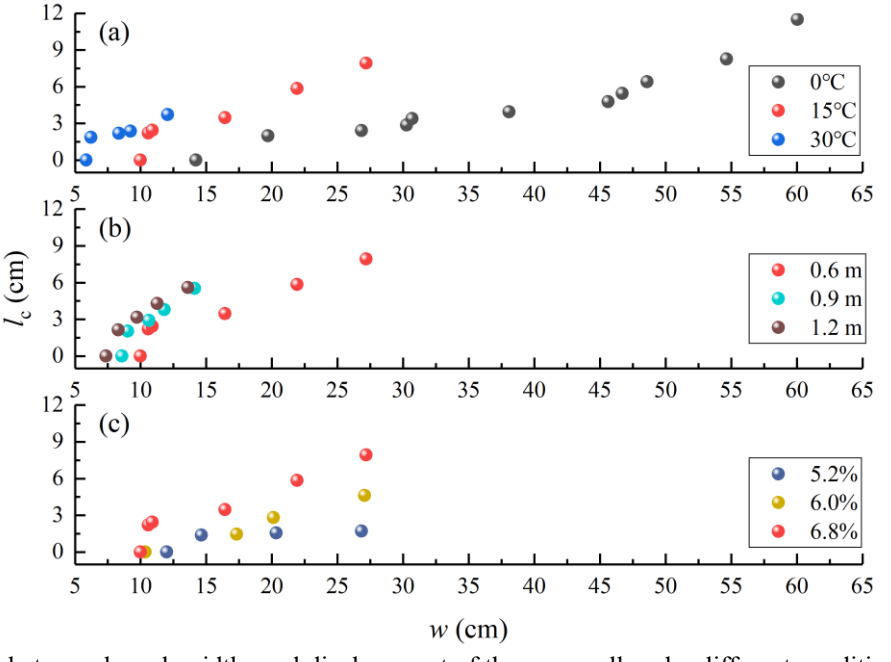

Fig. 10: The relationship between breach widths and displacement of the core wall under different conditions of (a) environmental temperature, (b) dam height, and (c) asphalt content in the core wall.

yielding dimensionless values for core wall displacement and breach development under different conditions. Arrows indicate the temporal progression of the process.

The results demonstrate that as the S1 group experiment progressed, the relative magnitude of the other groups' data compared to S1 gradually decreased. At 0 °C, where the high strength of the core wall led to greater displacement and breach expansion, all other groups exhibited smaller values than S1. In the case of different dam heights (0.9 m and 1.2 m), the breach expansion exhibited significant variations when compared to the S1 reference case, the breach did not undergo significant expansion due to the failure to reach the threshold depth. Low asphalt content primarily governs the displacement behavior of the core wall, the three groups exhibited comparable breach development patterns. However, due to the reduced strength of the core wall caused by the lower asphalt content, the normalized displacement of the core wall decreased significantly as the asphalt content diminished.

A fitting analysis is performed on the displacement at the center of the asphalt core wall under varying asphalt content and environmental temperature (Fig. 11). A formula is derived to express the maximum displacement of the asphalt core wall, incorporating the effects of asphalt content and temperature Eqs. (6) and (7):

$$e^{0.5d}=-771.94x+1052.9 \tag{6}$$

$$x=\log(1/a)+T/150 \tag{7}$$

where d is the displacement of the asphalt core wall (cm); a is the asphalt content in core wall (%); T is the environmental temperature (°C).

The results indicate that the maximum displacement of the core wall is strongly correlated with the asphalt content in the core wall and environmental temperature. The derived equation provides a quantitative means of determining the displacement of the asphalt concrete core wall under varying temperatures and asphalt content conditions.

5. A simplified numerical model for the asphalt concrete core wall failure process

Previous numerical studies on asphalt concrete core dams have primarily focused on material properties and breach process. Wang proposed a simplified material model to represent the response of asphalt cores under various loading conditions in embankment dams,[35] while Yang developed a numerical model to simulate the overtopping-induced breach process, considering the structural role of the core wall during dam failure.[7] In addition, some researchers have employed commercial software to investigate the seismic response of asphalt concrete core dams under earthquake loading.[36,37] These studies provide valuable insights into the stress distribution, deformation, and overall failure of dams; however, they offer limited description of the progressive structural damage and crack propagation within the core wall itself.

To address this gap, a simplified numerical model is developed in this study to analyze the initiation and evolution of cracks. The model is established under the following assumptions: (1) the asphalt concrete core is treated as an ideal viscoelastic material; and (2) the breach development is

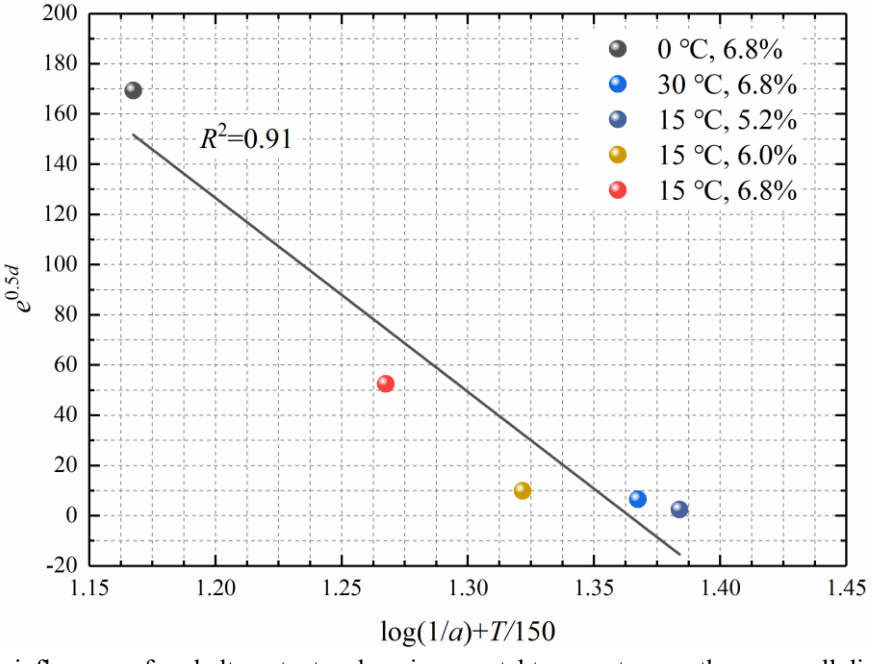

Fig. 11: The influences of asphalt content and environmental temperature on the core wall displacement.

derived from experimental statistical data, without considering the coupling between the core structure and sediment transport.

5.1 Quantitative analysis of the asphalt concrete core wall failure process

Unlike soil materials, the asphalt concrete core exhibits visco-plastic deformation under external loads. The failure of the core wall is governed by both the material properties of asphalt concrete and the principles of structural fracture mechanics. Considering these characteristics, a numerical method is proposed.

The failure process of the asphalt concrete core can be divided into three phases under the action of the overtopping flow (as shown in Fig. S16(a)): (1) the exposed core wall generates plastic deformation (Fig. S16(b)); (2) initial cracks appear in the core wall (Fig. S16(c)); (3) the crack length increases until the core wall fails (Fig. S16(d)). The numerical simulation of the failure process is described as follows:

5.1.1 Plastic deformation of the exposed core wall

The Burgers constitutive model effectively simulates the deformation of the core wall, which is described by the following Eq. (8):

$$\varepsilon(t)=\sigma\left[\frac{1}{E_1}+\frac{1}{\eta_1}t+\frac{1}{E_2}\left(1-e^{\frac{-E_2 t}{\eta_2}}\right)\right] \tag{8}$$

where σ is the applied stress, E_1 is the instantaneous elastic modulus; E_2 is the Kelvin elastic modulus; η_1 is the Maxwell viscosity coefficient; η_2 is the Kelvin viscosity coefficient.

5.1.2 Calculation of initial cracks

Initial cracks emerge when deformation in the core wall reaches a critical threshold. The initial crack length is calculated based on the principle of energy conservation. The primary energies involved in crack formation are (1) Strain energy (U), which is the energy stored in the structure due to external forces, and (2) Surface energy (γ), which is the energy required to create new surfaces during crack propagation.

The total energy change can be expressed by Eq. (9):

$$\Delta E=U-2\gamma A \tag{9}$$

where ΔE is the total change in energy; U is the strain energy; γ is the surface energy per unit area; A is the area of the new surfaces created by crack propagation.

Herein, U can be expressed as follows in Eq. (10):

$$U=\frac{1}{2}\int_V \sigma\varepsilon dV \tag{10}$$

The energy is conserved in the crack propagation process, so the total energy ΔE is 0. Hence, we get Eq. (11):

$$U=2\gamma A \tag{11}$$

Therefore, the initial crack length a can be expressed by Eq. (12):

$$a=\frac{1}{4\gamma}\sigma\varepsilon L \tag{12}$$

where a is the initial crack length; L is the length of the deformed structure; γ is the fracture stiffness.

5.1.3 Crack propagation and fracture of the core wall

Based on the fracture mechanism, the core wall undergoes Mode III (Tearing) failure. In fracture mechanics, the stress intensity factor (K_{III}) describes the stress field at the crack tip,[38,39] which depends on the loading conditions and the crack geometry. The formula for determining the stress intensity factor is in Eq. (13):

$$K_{\mathrm{III}}=\left(\tau_{\mathrm{w}}+\tau_{\mathrm{t}}\right)Y\sqrt{\pi a} \tag{13}$$

where τ_{w} is the frictional force of the flow within the crack; τ_{t} is the frictional force of the overtopping flow; Y is the shape factor.

The J-integral is a path-independent energy integral utilised to characterise the intensity of the stress and strain fields near the crack tip.[40] The J-integral formula is in Eq. (14):

$$J_{\mathrm{III}}=\int_{\Gamma}\left(W\mathrm{d}y-\sigma_{ij}\frac{\partial u_i}{\partial x_j}\mathrm{d}s\right) \tag{14}$$

where J_{III} is the J-integral value for Mode III; W is the strain energy density; σ_{ij} is the stress components; u_i is the displacement components; x_j and y are the coordinate components; ds is the differential length along the path.

The value in the initial state can be calculated using the following Eq. (15):

$$J_{\mathrm{III},0}=\frac{K^2_{\mathrm{III,initial}}}{E'} \tag{15}$$

where E' is equivalent elastic modulus under plane stress conditions; E' and E_1 are equal.

With the enlargement of the breach, J_{III} reaches or exceeds the critical value J_{c}, the crack will begin to propagate. Assuming a crack increment of Δa, the new crack length is $a+\Delta a$. The new stress intensity factor can be expressed as follows Eq. (16):[40]

$$K_{\mathrm{III},1}=(\tau_{\mathrm{w}}+\tau_{\mathrm{t}})Y\sqrt{\pi\left(a+\Delta a\right)} \tag{16}$$

The new J-integral is in Eq. (17),

$$J_{\mathrm{III},1} = \frac{K^2_{\mathrm{III},1}}{E'} \tag{17}$$

The condition for crack propagation is as follows in Eq. (18):

$$J_{\mathrm{III},1} > J_{\mathrm{c},1} \tag{18}$$

Due to crack propagation and the change in the plastic zone, the critical value for the new crack is in Eq. (19):

$$J_{\mathrm{c},1} = J_{\mathrm{c},0} + \alpha \cdot \Delta J_{\mathrm{p}} \tag{19}$$

where α is the material's hardening or softening coefficient; ΔJ_{p} is the additional J-integral due to changes in the plastic zone, which can be calculated using the following Eq. (20):

$$\Delta J_{\mathrm{p}} = \frac{K^2_{\mathrm{III},1}}{E'}\left(1 + \frac{E'}{E}\frac{r_{\mathrm{p}}}{a}\right) \tag{20}$$

where r_{p} is the radius of the plastic zone.

$$r_{\mathrm{p}} = \frac{1}{2\pi}\left(\frac{K}{\sigma_{\mathrm{y}}}\right)^2 \tag{21}$$

where σ_{y} is the material's yield strength.

The new crack propagation increment Δa can be expressed as follows Eq. (22):

$$\Delta a = \frac{J_{\mathrm{c},1}E'}{\left(\tau_{\mathrm{w}} + \tau_{\mathrm{t}}\right)^2 Y^2 \pi} - a \tag{22}$$

As the crack propagates, the exposed core wall is subjected to unbalanced water and soil pressures from upstream and downstream. The moment balance method is utilised to analyse the stability of the exposed core wall. The overturning and resisting moments acting on the core wall are calculated at each time step. The critical condition for overturning failure is described as follows Eq. (23):

$$M_{\mathrm{o}} = M_{\mathrm{r}} \tag{23}$$

where M_{o} is the overturning moment; M_{r} is the resistant moment.

The overturning moment action on the core wall is in Eq. (24):

$$M_{\mathrm{o}} = F_{\mathrm{s}} \cdot h_{\mathrm{k}} + F_{\mathrm{w}} \cdot \frac{h_{\mathrm{k}}\left(2h_{\mathrm{r}} - h_{\mathrm{k}}\right) + h_{\mathrm{r}}}{3\left(h_{\mathrm{r}} - h_{\mathrm{k}} + h_{\mathrm{r}}\right)} + F_{\mathrm{e}} \cdot \frac{h_{\mathrm{k}}\left(2h_{\mathrm{r}} - h_{\mathrm{k}}\right) + h_{\mathrm{r}}}{3\left(h_{\mathrm{r}} - h_{\mathrm{k}} + h_{\mathrm{r}}\right)} \tag{24}$$

where F_{s} is the flow shear stress at the top of core; F_{w} is the water pressure on the upstream of core wall; F_{e} is the soil pressure on upstream of the core wall; h_{k} is the height of the failed core wall; h_{r} is the depth between the reservoir water level and the failure plane of core wall.

The following formula (Eq. (25)) describes the moment of the resistant forces:

$$M_{\mathrm{r}} = 2A \cdot C \cdot \frac{h_{\mathrm{k}}\left(2h_{\mathrm{r}} - h_{\mathrm{k}}\right) + h_{\mathrm{r}}}{3\left(h_{\mathrm{r}} - h_{\mathrm{k}} + h_{\mathrm{r}}\right)} + \frac{1}{2}W \cdot L \tag{25}$$

where A is the surface area of the core wall; C is the cohesion of the core wall; W is the weight of the core wall above the failure plane.

When $M_{\mathrm{o}} > M_{\mathrm{r}}$, the force of the water and soil pressures from upstream acting at the core wall cause its failure. The specific calculation process is shown in Fig. S17.

5.2 Deformation and crack growth of core wall under different factors

Based on the deformation and failure model of asphalt concrete cores, a simplified numerical model is developed to simulate the process from exposure to failure of the core wall, incorporating considerations of wall deformation and fracture mechanics. The cohesion of asphalt concrete at different temperatures is determined using the following Eq. (26):[19]

$$\log c = 0.3454\left(\log \gamma - 0.104T + 1.04\right) + 0.8942 \tag{26}$$

where c is the cohesion; γ is the strain rate, and $\gamma = 0.0001$/s.

The following formulas (Eqs. (27) and (28)) represent the shear modulus and shear strength:

$$\log G = 0.4346\left(\log \gamma - 0.104T + 1.04\right) + 2.2690 \tag{27}$$

$$\log \tau_{\mathrm{f}} = 0.318\left(\log \gamma - 0.104T + 1.04\right) + 0.9272 \tag{28}$$

where G is the shear modulus; τ_{f} is the shear strength.

The strength reduction method is considered for different asphalt contents in the core walls. The main calculation parameters under different conditions are listed in Table 8.

5.2.1 Simulation on the deformation of the asphalt concrete core wall

The flowchart in Fig. S17 calculates the deformation, crack propagation, and failure processes of asphalt concrete core walls under various influencing factors (Table 9). If the horizontal axis represents the dam axis, the core wall deforms and bends towards the downstream direction. The calculated results are compared to experimental values. At different temperatures, the calculated maximum displacements of the core walls are 11.83 cm (at 0 °C), 8.01 cm (at 15 °C), and 4.14 cm (at 30 °C), compared to experimental values of 10.26 cm (at 0 °C), 7.92 cm (at 15 °C), and 3.72 cm (at 30 °C), with

relative errors of 15.30%, 1.14%, and 11.29%, respectively. For different dam heights, the calculated maximum displacements of the core walls are 5.48 cm (at 0.9 m) and 5.06 cm (at 1.2 m), compared to experimental values of 5.53 cm (at 0.9 m) and 5.60 cm (at 1.2 m), with relative errors of -0.90% and -9.64%, respectively. For different asphalt contents in the core walls, the calculated maximum displacements are 1.60 cm (at 5.2%) and 4.69 cm (at 6.0%), compared to experimental values of 1.70 cm (at 5.2%) and 4.60 cm (at 6.0%), with relative errors of -5.88% and 1.96%, respectively. The relative errors between the calculated results and experimental values under various factors do not exceed ±15%, indicating a reasonable correspondence between the numerical calculations and the actual measurements.

Table 8: Input parameters for the core walls under different conditions.

Parameter	Environmental temperature (℃)			Dam height (m)		Asphalt content in core wall (%)	
	0	15	30	0.9	1.2	5.2	6.0
E_1 (MPa)	9.61	2.02	0.42	2.02	2.02	1.61	1.81
E_2 (MPa)	100	80	60	80	80	48	64
η_1 (MPa·s)	2200	1800	1600	1800	1800	1080	1440
η_2 (MPa·s)	140	100	80	100	100	60	80
σ_y (MPa)	0.96	0.31	0.10	0.31	0.31	0.19	0.25
c (MPa)	0.33	0.09	0.21	0.09	0.09	0.05	0.07
G_f (J/m^2)	3	2	1	2	2	0.7	1

Table 9: Comparison of calculated and experimental value under different influencing factors.

No.	Calculated value (cm)	Experiment value (cm)	Relative error
S1	8.01	7.92	1.14%
T1	11.83	10.26	15.30%
T2	4.14	3.72	11.29%
H1	5.48	5.53	-0.90%
H2	5.06	5.60	-9.64%
A1	1.60	1.70	-5.88%
A2	4.69	4.60	1.96%

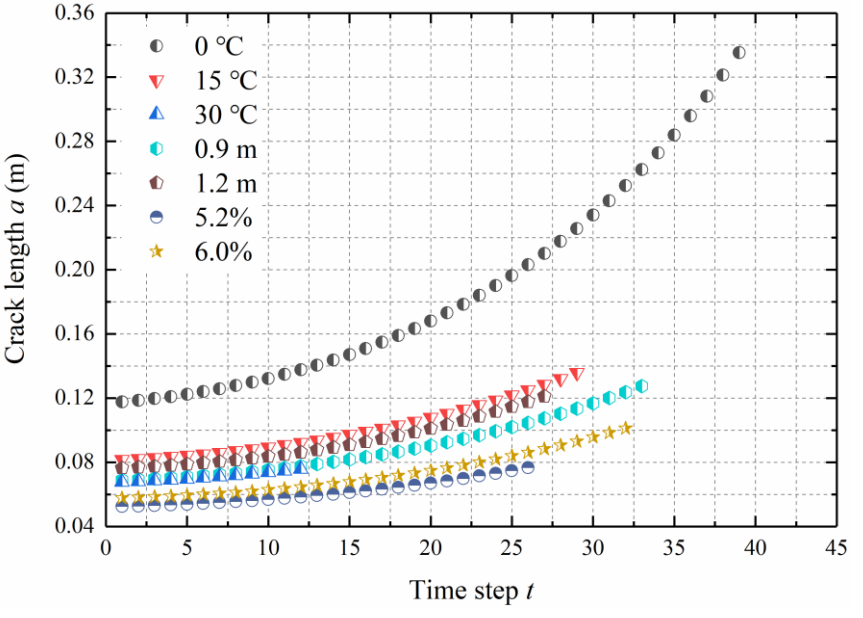

Fig. 12: Crack development processes in the asphalt concrete core walls.

5.2.2 Simulation on the crack development of the asphalt concrete core wall

Fig. 12 illustrates that with an increase in the exposed area of the core wall and the width of the breach, the overturning moment on the core wall increases, leading to an accelerated trend in crack growth. As the temperature rises, the elastic modulus, strength, and inherent cohesion of the asphalt concrete gradually decrease, reducing the length of the cracks. The final crack lengths at 0, 15, and 30 ℃ are 33.51, 13.78, and 7.58 cm, respectively. Using 15 ℃ as a reference, the crack lengths at 0 and 30 ℃ increased by 143.18% and decreased by 44.99%, respectively.

For different dam heights, as neither 0.9 nor 1.2 m reached the critical depth in the breach, the exposed depth of the core wall continuously increased while the growth of the breach width remained slow. Compared to a dam with a height of 0.9 m, the 1.2 m high dam exhibited a higher erosion rate alongthe depth, resulting in a greater breach depth. Therefore, the overturning moment was higher, leading to larger crack values. However, the final crack length was smaller than that at the dam height of 0.9 m. The final crack lengths for dam heights of 0.9 and 1.2 m are 12.94 and 12.11 cm, respectively, representing decreases of 6.10% and 12.12% compared to a 0.6 m high dam.

For different asphalt contents in the core walls, lower asphalt content results in lower strength and cohesion. The final crack lengths for asphalt contents of 5.2% and 6.0% are 7.67 and 10.26 cm, respectively, representing decreases of 44.34% and 25.54% compared to an asphalt content of 6.8%.

6. Conclusions

This study investigates the overtopping-induced breach mechanisms of ACCDs with low permeability downstream shells under various conditions. Seven model experiments are conducted in physical models with varying asphalt contents in core walls, environmental temperatures, and dam heights to analyze the breach processes, flow discharge, and failure mechanisms of asphalt concrete cores, among these factors, environmental temperature proves to be the most sensitive, exerting the strongest influence on both the timing and magnitude of breach development. A simplified numerical model, integrating the Burgers model, the principle of energy conversion, and fracture mechanics, is developed based on the experimental outcomes. The main conclusions are as follows:

(1) Based on model experiments, the breach process of an ACCD is divided into three stages: in Stage I, erosion on the downstream slope until the asphalt concrete core is exposed; in Stage II, multiple fractures of the core wall occur until the peak breach flow is reached; in Stage III, the decline in breach flow until breach morphology stabilizes. The strength of the core wall is significantly influenced by various factors, which directly impact the elapsed time of Stage I.

(2) The results demonstrate that asphalt content, environmental temperature, and dam height exert distinct influences on breach development: higher asphalt content enhances resistance and reduces peak breach flow, elevated temperature accelerates failure, with magnitude strongly linked to the time to peak and upstream water level. Increasing dam height leads to larger peak breach flow, while the time to peak remains nearly unchanged.

(3) Low asphalt content and high environmental temperature weaken the strength of the asphalt concrete core wall, resulting in small breach size and core wall displacement. Based on the experimental results of core wall displacement, a predictive formula for the core wall displacement is developed that considers different asphalt contents and temperatures.

(4) In Stage I, the development of the breach in the coarse-grained materials progresses vertically downwards until it reaches a threshold depth, after which it expands laterally. Higher dam height leads to the failure of the core wall before the breach reaches the threshold depth, resulting in a deep and narrow breach.

(5) A simplified numerical model is developed to simulate the deformation and fractures process. The Burgers model to simulate the deformation of the asphalt concrete core wall; the model calculates the initial crack length based on the principle of energy conversion and estimates the crack growth process using fracture mechanics. The calculated results align well with the experimental findings.

Data availability

Some or all data, models, or code that support the findings of this study are available from the corresponding author upon reasonable request.

Acknowledgments

This work has been financially supported by the National Natural Science Foundation of China (Grant Nos. U22A20602, U24A20182, and 52409138), the Fundamental Research Funds for Central Public Research Institutes (Grant Nos. Y324006 and Yk325002), and the China Scholarship Council program (Grant Nos. 202308320446).

Conflict of Interest

There is no conflict of interest.

Supporting Information

Applicable.

CRediT Statement

Meng Yang: Investigation, Methodology, Data curation, Formal analysis, Original draft, Funding acquisition. **Qiming Zhong**: Conceptualization, Methodology, Project administration, Writing – review & editing, Supervision, Funding acquisition. **Liang Hu**: Data curation, Methodology. **Lucheng Zhang**: Investigation, Data curation. **Rafael Morán**: Writing – review & editing, Supervision. **Ignacio González**: Writing – review & editing, Supervision. **Miguel Á. Toledo**: Writing – review & editing, Supervision.

Reference

[1] Q. Zhong, W. Wu, S. Chen, M. Wang, Comparison of simplified physically based dam breach models, *Natural Hazards*, 2016, **84**, 1385-1418, doi: 10.1007/s11069-016-2492-9.

[2] ASCE/EWRI Task Committee on Dam/Levee, Breaching Earthen embankment breaching, *Journal of Hydraulic Engineering*, 2011, **137**, 1549-1564, doi: 10.1061/(asce)hy.1943-7900.0000498.

[3] Q. Zhong, L. Wang, S. Chen, Z. Chen, Y. Shan, Q. Zhang, Q. Ren, S. Mei, J. Jiang, L. Hu, J. Liu, Breaches of embankment and landslide dams - State of the art review, *Earth-Science Reviews*, 2021, **216**, 103597, doi: 10.1016/j.earscirev.2021.103597.

[4] Z. Zhang, W. Xu, W. Xia, H. Zhang, Large-scale *in situ* test for mechanical characterization of soil–rock mixture used in an embankment dam, *International Journal of Rock Mechanics and Mining Sciences*, 2016, **86**, 317-322, doi: 10.1016/j.ijrmms.2015.04.001.

[5] Q. Zhong, S. Chen, Z. Deng, A simplified physically-based model for core dam overtopping breach, *Engineering Failure Analysis*, 2018, **90**, 141-155, doi: 10.1016/j.engfailanal.2018.03.032.

[6] H. Zhang, J. Chen, S. Hu, Y. Xiao, B. Zeng, Deformation characteristics and control techniques at the shiziping earth core rockfill dam, *Journal of Geotechnical and Geoenvironmental Engineering*, 2016, **142**, 04015069, doi: 10.1061/(asce)gt.1943-5606.0001385.

[7] M. Yang, Q. Zhong, L. Hu, Y. Li, H. Lu, Model tests and numerical simulation of overtopping-induced breach process of the asphalt concrete core dam, *Engineering Failure Analysis*, 2024, **157**, 107877, doi: 10.1016/j.engfailanal.2023.107877.

[8] W. B. Wang, Development and applications of impervious asphalt concrete for embankment dams, *Journal of Hydroelectric Engineering*, 2004, **23**, 70-74.

[9] H. Li, J. Yu, S. Wu, Q. Liu, Y. Wu, H. Xu, Y. Li, Effect of moisture conditioning on mechanical and healing properties of inductive asphalt concrete, *Construction and Building Materials*, 2020, **241**, 118139, doi: 10.1016/j.conbuildmat.2020.118139.

[10] Y. Zhang, K. Höeg, W. Wang, Y. Zhu, Watertightness, cracking resistance, and self-healing of asphalt concrete used as a water barrier in dams, *Canadian Geotechnical Journal*, 2013, **50**, 275-287, doi: 10.1139/cgj-2011-0443.

[11] W. Pircher, H. Schwab, Austria's finstertal rockfill dam, *International Journal of Rock Mechanics and Mining Sciences & Geomechanics Abstracts*, 1981, **18**, 14, doi: 10.1016/0148-9062(81)90430-7.

[12] S. Feng, W. Wang, W. Hu, Y. Deng, J. Yang, S. Wu, C. Zhang, K. Höeg, Design and performance of the Quxue asphalt-core rockfill dam, *Soils and Foundations*, 2020, **60**, 1036-1049, doi: 10.1016/j.sandf.2020.06.008.

[13] W. Wang, K. Höeg, Y. Zhang, Design and performance of the Yele asphalt-core rockfill dam, *Canadian Geotechnical Journal*, 2010, **47**, 1365-1381, doi: 10.1139/t10-028.

[14] L. Yu, X. Jin, Z. Ding, Experimental study on factors of dynamic properties of core wall asphalt concrete, *Journal of Hydroelectric Engineering*, 2013, **32**, 194-198, doi: CNKI:SUN:SFXB.0.2013-03-034.

[15] G. P. Piuzzi, H. C. Scheuermann Filho, J. A. Villena Del Carpio, N. C. Consoli, The effects of porosity, asphalt content and fiberglass incorporation on the tensile strength and resilient modulus of asphalt concrete blends, *Geotextiles and Geomembranes*, 2021, **49**, 864-870, doi: 10.1016/j.geotexmem.2021.01.002.

[16] Z. Ning, Y. Liu, W. Wang, J. Dong, X. Meng, Experimental study on effect of temperature on direct tensile behavior of hydraulic asphalt concrete at different strain rates, *Journal of Materials in Civil Engineering*, 2022, **34**, 04022143, doi: 10.1061/(asce)mt.1943-5533.0004295.

[17] G. Xu, H. Wang, Molecular dynamics study of interfacial mechanical behavior between asphalt binder and mineral aggregate, *Construction and Building Materials*, 2016, **121**, 246-254, doi: 10.1016/j.conbuildmat.2016.05.167.

[18] Z. Xu, Y. Wang, J. Cao, J. Chai, C. Cao, Z. Si, Y. Li, Adhesion between asphalt molecules and acid aggregates under extreme temperature: a ReaxFF reactive molecular dynamics study, *Construction and Building Materials*, 2021, **285**, 122882, doi: 10.1016/j.conbuildmat.2021.122882.

[19] W. Wang, K. Hu, S. Feng, G. Li, K. Höeg, Shear behavior of hydraulic asphalt concrete at different temperatures and strain rates, *Construction and Building Materials*, 2020, **230**, 117022, doi: 10.1016/j.conbuildmat.2019.117022.

[20] Z. Ning, Y. Liu, W. Wang, Compressive behavior of hydraulic asphalt concrete under different temperatures and strain rates, *Journal of Materials in Civil Engineering*, 2021, **33**, 04021013, doi: 10.1061/(asce)mt.1943-5533.0003594.

[21] S. Yu, Q. Zhang, Z. Chen, J. Hao, L. Wang, P. Li, Q. Zhong, Study of the Sheyuegou dam breach–Experience with the post-failure investigation and back analysis, *Engineering Failure Analysis*, 2021, **125**, 105441, doi: 10.1016/j.engfailanal.2021.105441.

[22] J. Zhang, Y. Li, G. Xuan, X. Wang, J. Li, Overtopping breaching of cohesive homogeneous earth dam with different cohesive strength, *Science in China Series E: Technological Sciences*, 2009, **52**, 3024-3029, doi: 10.1007/s11431-009-0275-1.

[23] R. Monteiro-Alves, R. Moran, M. Á. Toledo, J. Peraita, Structural failure of the cohesive core of rockfill dams: an experimental research using sand-bentonite mixtures, *Water*, 2022, **14**, 3966, doi: 10.3390/w14233966.
[24] M. Á. Toledo, R. Monteiro-Alves, R. Morán, Structural failure of the clay core or the upstream face of rockfill dams in overtopping scenario, *Dam Protections against Overtopping and Accidental Leakage*, CRC Press, 2015, 101-109, doi: 10.1201/b18292.
[25] K. Zhao, Q. Zhong, S. Chen, H. Wu, Y. Shan, B. Qian, P. Jing, Y. Chao, Experimental study on overtopping failure of concrete face rockfill dam, *Case Studies in Construction Materials*, 2024, **21**, e03640, doi: 10.1016/j.cscm.2024.e03640.
[26] P. Ding, To choice the aggregate grading of asphalt concrete in hydraulic engineering. *Journal of Xi'an University of Technology*. 1990, **6**, 250-258, doi: 10.19322/j.cnki.issn.1006-4710.1990.04.004.
[27] J. Fu, S. Jin, A study on unsteady seepage flow through dam, *Journal of Hydrodynamics, Ser. B*, 2009, **21**, 499-504, doi: 10.1016/S1001-6058(08)60176-6.
[28] D. Hansen, W. Z. Zhao, S. Y. Han, Hydraulic performance and stability of coarse rockfill deposits, *Proceedings of the Institution of Civil Engineers - Water Management*, 2005, **158**, 163-175, doi: 10.1680/wama.2005.158.4.163.
[29] B. Li, V. K. Garga, M. H. Davies, Relationships for non-darcy flow in rockfill, *Journal of Hydraulic Engineering*, 1998, **124**, 206-212, doi: 10.1061/(asce)0733-9429(1998)124:2(206).
[30] R. Monteiro-Alves, M. Á. Toledo, R. Morán, Characterization of the overtopping flow through the downstream shell of rockfill dams, *Journal of Hydraulic Engineering*, 2019, **145**, 04019015, doi: 10.1061/(asce)hy.1943-7900.0001598.
[31] M. A. Toledo, Presas de Escollera Sometidas a Sobrevertido. Estudio Del Movimientos Dal Agua a Través de la Escollera Y de la Estabilidad Frente Al Deslizamiento En Masa (Ph.D. thesis), Universidad Politécnica de Madrid; 1997.
[32] A. Larese, R. Rossi, E. Oñate, M. Á. Toledo, R. Morán, H. Campos, Numerical and experimental study of overtopping and failure of rockfill dams, *International Journal of Geomechanics*, 2015, **15**, 04014060, doi: 10.1061/(asce)gm.1943-5622.0000345.
[33] I. González Tejada, R. Monteiro-Alves, R. Morán, M. Á. Toledo, Cellular automata modeling of rockfill dam failure caused by overtopping or any other extreme throughflow, *Engineering Structures*, 2021, **245**, 112933, doi: 10.1016/j.engstruct.2021.112933.
[34] Y. Bi, F. Guo, J. Zhang, J. Pei, R. Li, Correlation analysis between asphalt binder/asphalt mastic properties and dynamic modulus of asphalt mixture, *Construction and Building Materials*, 2021, **276**, 122256, doi: 10.1016/j.conbuildmat.2021.122256.
[35] W. Wang, K. Höeg, Simplified material model for analysis of asphalt core in embankment dams, *Construction and Building Materials*, 2016, **124**, 199-207, doi: 10.1016/j.conbuildmat.2016.07.077.
[36] S. Feizi-Khankandi, A. Ghalandarzadeh, A. Mirghasemi, K. Hoeg, Seismic analysis of the garmrood embankment dam with asphaltic concrete core, *Soils and Foundations*, 2009, **49**, 153-166, doi: 10.3208/sandf.49.153.
[37] B. Sun, M. Deng, S. Zhang, C. Wang, M. Du, Seismic performance assessment of high asphalt concrete core rockfill dam considering shorter duration and longer duration, *Structures*, 2022, **39**, 1204-1217, doi: 10.1016/j.istruc.2022.03.040.
[38] P. C. Paris, G. C. Sih, Fracture toughness testing and its applications, *ASTM Special Technical Publication*, 1965, **381**, 30-81, doi: 10.1520/STP26584S.
[39] G. R. Irwin, Analysis of stresses and strains near the end of a crack traversing a plate, *Journal of Applied Mechanics*, 1957, **24**, 361-364, doi: 10.1115/1.4011547.
[40] J. R. Rice, A path independent integral and the approximate analysis of strain concentration by notches and cracks, *Journal of Applied Mechanics*, 1968, **35**, 379-386, doi: 10.1115/1.3601206.